

CONSTRUCTING A PYTHON PIPELINE FOR ANALYZING SPATIALLY RESOLVED ALMA OBSERVATIONS OF IRAS 16293-2422

J. L. CAMPBELL^{1,2}, MAGNUS PERSSON³, AND MIHKEL KAMA³

Draft version August 28, 2015

ABSTRACT

We discuss the results of a Python pipeline written to analyse high quality ALMA data of the deeply-embedded low-mass protostar IRAS 16293-2422. The emission is spatially resolved, providing a unique insight into the morphology of the complex organic molecules abundant in hot corino objects. We investigate detections of 97 pure rotational transitions of CH₃CHO (acetaldehyde), 18 transitions of CH₃OH (methanol), and 50 transitions of CH₃OCHO (methyl formate) above a 5σ level. Using an LTE model, acetaldehyde and methanol are found at local standard-of-rest velocities of $v_{\text{LSR}} = 2.7 \text{ km s}^{-1}$, while methyl formate is found at $v_{\text{LSR}} = 4.7 \text{ km s}^{-1}$. The tasks performed by the Python pipeline to analyse the data includes creating noise maps as well as integrated line intensity, velocity, and velocity dispersion maps of all detected rotational transitions. We find no trend with E_{ul} and v_{LSR} nor E_{ul} and σ_v . We do however find a correlation between σ_v and v_{LSR} for $v > v_{\text{LSR}}$, and an anti-correlation for $v < v_{\text{LSR}}$, likely the result of line-blending. Column density maps of each detected transition (N_{ul}^{thin}) are also created for regions excluding absorption with the assumption that the emission is optically thin. Using the population diagram technique, which consists of plotting N_{ul}^{thin} per statistical weight as a function of the upper-level energy, total column density (N_{tot}) and rotational (excitation) temperature (T_{rot}) maps are created for the three molecules. Restricting these maps to 5σ measurements using the fit uncertainties still result in regions of non-physical (i.e., negative) temperatures and unusually high column densities, so they are confined to regions satisfying $0 \text{ K} < T_{\text{rot}} < 2500 \text{ K}$. Further investigation is required to determine whether this is the result of the gas being in non-LTE, in which case the population diagram technique would be an inadequate approximation. Analysing the spatial distribution of the emission in the N_{tot} and T_{rot} maps indicates that, while acetaldehyde and methyl formate have somewhat extended emission, methanol is found to be particularly compact. This may however be due to the lower detection rate of methanol. The combination of line blending and ALMA’s small beam size cannot explain the extent to which observed N_{tot} are higher than previously found, thus further investigation is required. The median T_{rot} found for acetaldehyde is 254 K, and is consistent with previous studies. Median T_{rot} values for methanol and methyl formate are 1,189 K and 307 K, respectively.

1. INTRODUCTION

Low-mass stars are believed to form through the gravitational collapse of over-densities in the interstellar medium (ISM) located in the coldest and densest regions of molecular clouds (e.g., Myers 1985). The details of the subsequent evolution of these so-called dense cores from starless to their protostellar counterparts remains one of the largest controversies in star formation research, establishing the need for both observational and theoretical studies of young stellar objects (YSOs). Understanding the chemical enrichment that occurs as dense cores evolve is an active area of research as its role in the star formation process is poorly understood. Chemically-rich environments around some YSOs called “hot corinos” are the low-mass counterpart to high-mass “hot cores” that are characterized by warm temperatures ($T \geq 100 \text{ K}$), high densities ($n \geq 10^6 \text{ cm}^{-3}$) (Cazaux et al. 2003), and a rich inventory of molecular species

not abundant in dark molecular clouds (Walmsley et al. 1992). Continuum studies of chemically-rich protostellar envelopes have indicated a spatial offset in the emission of complex organic molecules from the peak of the dust continuum emission in some YSOs (e.g., Chandler et al. 2005), suggesting the need for an alternative explanation to the hot corino hypothesis to explain the origin of complex organics in YSO environments. Additionally, the question of whether observed complex organics are first generation molecules that are created in icy dust-grain mantles and are subsequently sublimated into the gas phase, or second generation molecules that are the result of grain-mantle evaporation followed by rapid gas phase reactions, remains an open debate today for many molecular species (Bisschop et al. 2008).

The connection between various molecular species has previously been studied by comparing molecular abundances in a large number of sources using single-dish radio telescopes (e.g., van der Tak et al. 2000). More recently, the high spatial resolution provided by radio interferometry has made studying the spatial distribution of molecular species possible, which allows for a better identification of where the emission is coming from (e.g., Bisschop et al. 2008). Spatially resolved molecular emission could not only assist in elucidating the origin of the chemical enrichment of the gas phase (i.e., whether com-

jessicalynn.campbell@mail.utoronto.ca

¹ Department of Astronomy & Astrophysics, University of Toronto, Canada.

² Leiden/ESA Astrophysics Program for summer Students (LEAPS), Leiden Sterrewacht (Observatory), Leiden University, The Netherlands.

³ Leiden Sterrewacht (Observatory), Leiden University, The Netherlands.

Table 1
Summary of ALMA Observations

spw Sidebands (1)	ν (GHz) (2)	ν_0 (GHz) (3)	Δv (km s ⁻¹) (4)	Ω (arcsec ²) (5)	Sensitivity (Jy beam ⁻¹ channel ⁻¹) (6)
0a	703.25 – 704.18	703.3125	0.416	0.053	0.017
0b	704.18 – 705.10	703.3125	0.419	0.054	0.121
1a	692.16 – 691.12	692.2375	0.423	0.057	0.093
1b	691.23 – 690.30	692.2375	0.424	0.057	0.095
2a	690.36 – 689.43	690.4375	0.424	0.057	0.092
2b	689.43 – 688.50	690.4375	0.425	0.058	0.091
3a	688.36 – 687.43	688.4375	0.426	0.059	0.094
3b	687.43 – 686.50	688.4375	0.426	0.059	0.091

Table 2
Summary of Detected Transitions

Molecular Species (1)	n_{lines} (2)	E_{ul} (K) (3)	A_{ul} (s ⁻¹) (4)	g_{ul} (5)
CH ₃ CHO	97	69.48 – 998.81	4.25×10^{-8} – 1.13×10^{-2}	30–170
CH ₃ OH	18	154.25 – 990.87	2.71×10^{-9} – 1.88×10^{-3}	17–62
CH ₃ OCHO	50	257.75 – 998.82	5.50×10^{-6} – 4.86×10^{-3}	74–218

plex molecules are first- or second-generation species), but also in allowing for a test of the hot corino hypothesis by searching for spatial correlations with continuum emission, protoplanetary disks, outflows, or other energy sources which could be (shock-) heating the gas. Studies of complex organics in star forming regions also serves as useful tracers for the physical conditions of star forming environments, such as their temperature, density, and velocity profiles, as well as indicators of their lifetime, evolutionary phase, and chemical complexity (Herbst & van Dishoeck 2009).

In this paper, we discuss a Python pipeline that was constructed to analyze high quality radio data of chemically-rich sources with spatially-resolved emission and an abundance of molecular lines. We review the results of IRAS 16293-2422 using publicly available Atacama Large Millimeter/submillimeter Array (ALMA) data, while focusing on a small subset of the molecular species present: acetaldehyde (CH₃CHO), methanol (CH₃OH), and methyl formate (CH₃OCHO). Details on the IRAS 16293-2422 source are discussed in Section 2, while ALMA observations are outlined in Section 3. The details of the Python pipeline are presented in Section 4. We discuss the results in Section 5, which includes some future work discussion on features that will be implemented into the Python pipeline. A summary is presented in Section 6, which includes a list of the tasks that the Python pipeline completes to analyse the high quality ALMA data.

2. IRAS16293-2422

IRAS 16293-2422, hereafter IRAS 1624, is a solar-type protostar in its early stage of formation located in the ρ Ophiuchi molecular cloud complex in the Ophiuchus molecular cloud. This exemplary candidate for astrochemical studies has a rich inventory of molecular species (e.g., Walker et al. 1986; Bisschop et al. 2008) and is a deeply-embedded Class 0 protostar, which are protostars defined to be in their earliest stage of formation

such that $M_* \ll M_{\text{env}}$ and $T_d \lesssim 20$ K (Andre et al. 1993). This source was one of the first protostellar systems identified as a binary candidate using dust continuum maps (Mundy et al. 1986), indicating a Southeastern “A” source and a Northwestern “B” source, hereafter IRAS A and IRAS B, respectively. The two components of IRAS A have a source separation of 0''.3, with IRAS B having a separation from IRAS A of 5'' (Mundy et al. 1986; Wootten 1989). At a distance of 160 parsecs, these angular separations correspond to physical distances of 48 AU and 800 AU, respectively. IRAS B is located at a right ascension of 16^h32^m22^s.61597 and a declination of $-24^\circ 28' 32''.496462$.

Both of the IRAS A and B components have been found to contain a wealth of molecules in their circumstellar envelopes (e.g., Bisschop et al. 2008). However there remain important differences between the two sources. Spectral observations by Jørgensen et al. (2011) found IRAS A and IRAS B to have average local-standard-of-rest velocities (v_{LSR}) of 3.2 km s⁻¹ and 2.7 km s⁻¹, and average velocity dispersions (σ_v) of 2.6 km s⁻¹ and 1.9 km s⁻¹, respectively. Using a standard T test for distributions with different variances, they found the v_{LSR} and σ_v distributions to be significantly different. Jørgensen et al. also found many Nitrogen- and Sulfur-bearing species to be predominantly detected towards IRAS A, with Oxygen-bearing complex organics to be more strongly detected towards IRAS B. The wealth of differences between the two sources indicates strong evidence for different physical environments likely to the result of being at different stages of evolution or evolving in different environments. IRAS A is known to be driving two bipolar outflows (see Mundy et al. 1992; Walker et al. 1988), while IRAS B presents clear indications of infall (e.g., Pineda et al. 2012). While IRAS A is generally agreed upon to be a protostar, the nature of IRAS B remains debated. Some authors have suspected IRAS B to be a prestellar core (i.e., a starless core expected

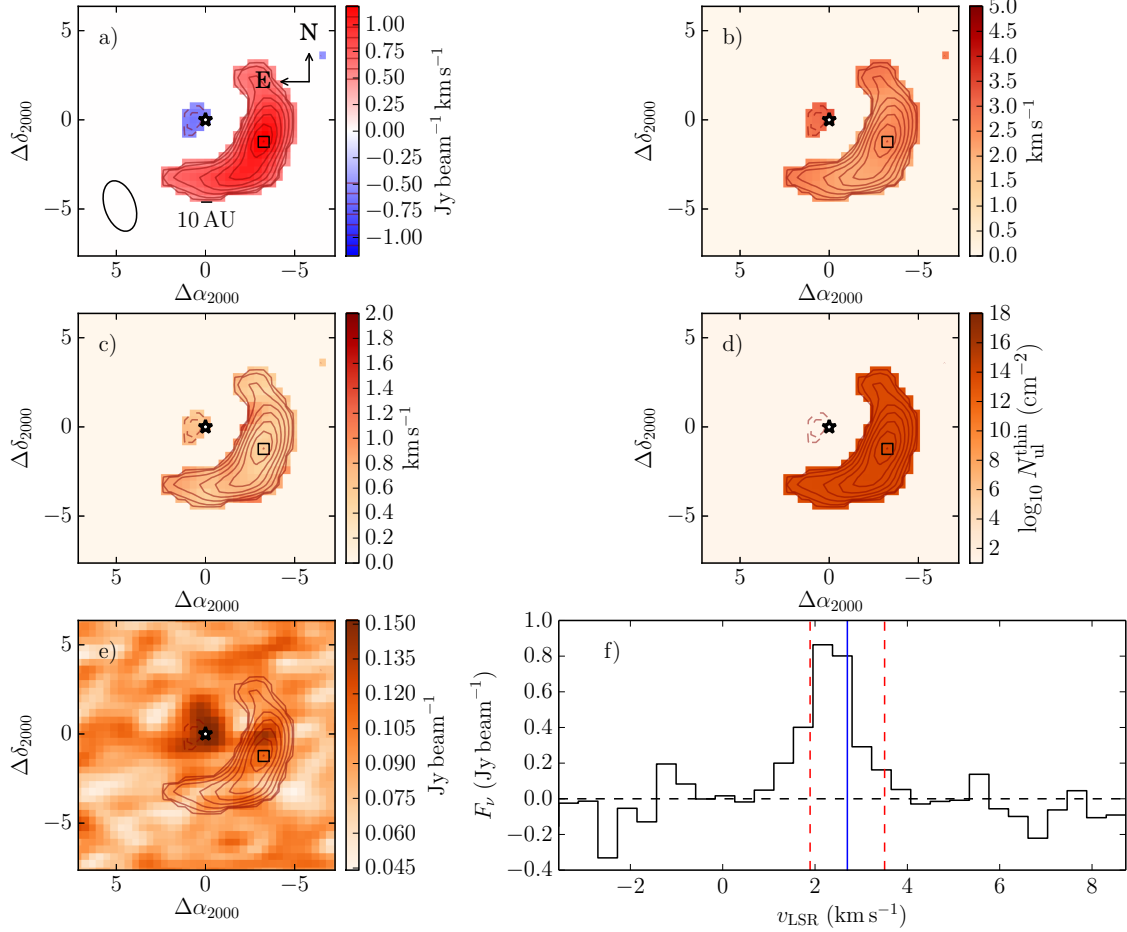


Figure 1. Emission of a rotational transition of Acetaldehyde in IRAS B with Quantum Numbers (21 318 2), an upper-level energy $E_{ul}=235.36$ K, and an Einstein A coefficient $A_{ul} = 3.49 \times 10^{-4}$ s⁻¹. The (black) star symbol indicates the pointing position of the IRAS B protostar, and the (black) square indicates the region with the strongest emission, corresponding to the spectrum shown in (f). Contours are those of the moment 0 map. (a) Moment 0 (μ_0) map, displaying the integrated line intensity. The beam size is shown in the bottom left corner, and 10 AU is shown to scale. (b) Moment 1 (μ_1) map, displaying the average velocity of the emission. (c) Moment 2 (μ_2) map, displaying the velocity dispersion of the emission. (d) Column density (N_{ul}^{thin}) of the transition. Note that N_{ul}^{thin} was determined for regions excluding absorption corresponding to the blue spatial region in (a). (e) Noise (rms) map of the spectral window. (f) Emission spectrum of the brightest spatial pixel, indicated by the (black) square. The (blue) solid vertical line is the v_{LSR} of the molecule, and the (red) dashed vertical lines are the $\pm 1.5\sigma$ velocity range that was used to calculate the maps in (a) – (d).

to form a protostar) (Chandler et al. 2005), while others argue that IRAS B is a T Tauri star (Stark et al. 2004).

IRAS 1624 presents itself as a unique opportunity to study the earliest stages of the formation of (high multiplicity) protostellar systems, infalling circumstellar envelopes, molecular outflows and shocks, as well as the wealth of molecular chemistry present in these environments.

3. ALMA OBSERVATIONS

Spectral observations of IRAS 1624 were taken with the Atacama Large Millimeter/submillimeter Array (ALMA) on April 16, 2012. The antenna configuration used was such that 15 antennas covered 105 independent baselines ranging from 26 – 402 m. The data was obtained in four spectral windows (spw), each one having an “a” and “b” sideband, resulting in 1900 spectral channels and a 1.86 GHz bandwidth in each spw. With a spectral resolution of $\Delta\nu = 976.46$ kHz and rest frequencies ranging from $\nu_0 = 688.4375 - 703.3125$ GHz, the cor-

responding velocity resolution ranged from $\Delta v = 0.416 - 0.426$ km s⁻¹. To estimate the level of noise in each spw, the baseline rms was measured in frequency ranges where no emission could be seen by eye for each independent spw. The sensitivity of the observations ranged from 0.017 – 0.121 Jy beam⁻¹ channel⁻¹. Table 1 summarizes the ALMA observations.

4. CONSTRUCTING A PYTHON PIPELINE

To analyze the high spectral and spatial resolution data provided by ALMA, a pipeline was written in Python to perform several tasks; this section outlines these tasks. Section 4.1 discusses the catalogs used to determine molecular emission lines present in the data, with the determination of detections discussed in Section 4.2. The analysis of moment maps are outlined in Section 4.3, with moment 0 maps discussed in Section 4.3.1, moment 1 maps in Section 4.3.2, and moment 2 maps in Section 4.3.3. The use of the population diagram technique is outlined in Section 4.4, which includes the total column

density and the rotational temperature of each molecule.

The current section outlines the details of the pipeline in the context of three complex organic molecules: acetaldehyde (CH_3CHO), methanol (CH_3OH), and methyl formate (CH_3OCHO).

4.1. JPL and CDMS Queries

To determine pure rotational molecular transitions that are present in the observed frequency ranges of each spw, NASA’s Jet Propulsion Laboratory (JPL) Molecular Spectroscopy database⁴ as well as the Cologne Database for Molecular Spectroscopy (CDMS) database⁵ were both queried using a Python code written by Sebastien Maret and Pierre Hily-Blant, complemented with another written by Mihkel Kama. The Splatalogue database for Astronomical Spectroscopy⁶ was not used to query the JPL and CDMS catalogs since many transitions were found to be missing, likely because the most updated databases were not available with Splatalogue at that time. Constraints on the Einstein A coefficient (A_{ul} ; related to the rate of spontaneous emission) and the upper-level energy used were $A_{ul} > 10^{-5} \text{ s}^{-1}$ and $E_{ul} < 1000 \text{ K}$. Energies in units of Kelvin were converted into units of cm^{-2} using the relationship $E(\text{K}) = 10^{-2}(k/hc)E(\text{cm}^{-2})$. A total of 220 acetaldehyde, 32 methanol, and 116 methyl formate rotational transitions were found in the frequency ranges covered by the observations.

4.2. Detections

A Local Thermodynamic Equilibrium (LTE) model was used on a few averaged spectra to estimate the v_{LSR} of each molecule. While acetaldehyde and methanol were found to have local standard-of-rest velocities of $v_{\text{LSR}} = 2.7 \text{ km s}^{-1}$ that agree with Jørgensen et al. (2011), methyl formate was found at $v_{\text{LSR}} = 4.7 \text{ km s}^{-1}$. Using these source velocities, the rest frequency of each molecular transition (ν_0) was converted to a local standard-of-rest frequency (ν_{LSR}) following the radio definition,

$$\nu_{\text{LSR}} = \left(1 - \frac{v_{\text{LSR}}}{c}\right) \nu_0, \quad (1)$$

which was then used to search for the location of the emission lines in the data. Assuming a FWHM of 1.9 km s^{-1} (Jørgensen et al. 2011) for IRAS B, the line identification and analysis was made over a velocity interval of $\pm 1.5\sigma$ about the measured systemic velocity of each emission line, which corresponds to a velocity range of $\pm 2.42 \text{ km s}^{-1}$. Converting the dispersion in velocity to frequency via

$$\sigma_\nu = \left(\frac{\sigma_v}{c}\right) \nu_{\text{LSR}}, \quad (2)$$

the frequency range within which the molecular transition is located was determined. Once the location and frequency range of each emission line was determined, the data was converted into a local standard-of-rest velocity using Equation 1.

⁴ <http://spec.jpl.nasa.gov/>

⁵ <https://www.astro.uni-koeln.de/cdms/catalog>

⁶ <http://www.splatalogue.net>

Possible line blending of crowded molecular emission lines was an important obstacle in determining the frequency/velocity range defined to encompass each emission line. While we assume a constant velocity dispersion across the entire source, performing more rigorous LTE modeling in various regions of the source would help to determine the linewidth of each line while adjusting for possible spatial variations and may help to correct for possible line blending. Jørgensen et al. (2011) find average FWHM values to vary from $\sim 0.5 \text{ km s}^{-1}$ to $\sim 5.5 \text{ km s}^{-1}$ for IRAS B, indicating a clear spatial variation in linewidth.

We set a signal-to-noise ratio (SNR) > 5 in integrated line intensity (W) for a source detection (see Equation 6). We detect 97/220 (44%) acetaldehyde transitions, 18/32 (56%) methanol transitions, and 50/116 (43%) methyl formate transitions above the 5σ level. The transitions of acetaldehyde cover excitation energies from 69 K to 999 K, with methanol covering 154 K to 991 K and methyl formate from 258 K to 999 K. The median excitation energy of acetaldehyde detected was 586 K, with that of methanol being 742 K and 483 K for methyl formate. Table 2 summarizes the detection rate of each molecule. Tables A.1, A.2, and A.3 in the Appendix lists all of the detections for acetaldehyde, methanol, and methyl formate, respectively.

4.3. Moment Maps

Moment maps are useful tools for analyzing radio emission data, providing an effective way to study the gas component of the ISM and its kinematics. The general definition of the moment is

$$\mu_n = \int_{-\infty}^{\infty} (x - a)^n f(x) dx. \quad (3)$$

In the context of radio astronomy, the variables of interest are velocity, v , and line intensity, $I(v)$, leading to the following more practical definition for radio astronomy,

$$\mu_n = \int_{-\infty}^{\infty} v^n I(v) dv, \quad (4)$$

where n indicates the order of the moment. The zeroth, first, and second moments of each of the three molecules were calculated in spatial regions with 5σ detections in W , and are discussed in the following sections.

4.3.1. Moment 0 Maps

The zeroth moment (μ_0) quantifies the integrated line intensity, and is calculated by setting $n = 0$ in Equation 4,

$$\mu_0 = \int_{-\infty}^{\infty} I(v) dv. \quad (5)$$

Discretizing Equation 5 for sampled spectral data, the zeroth moment is better referred to as the integrated line intensity (W) and is calculated as follows:

$$W = \sum_{-\infty}^{\infty} I(v) \Delta v. \quad (6)$$

Here, $I(v)$ is the flux density of the emission line at each spectral channel in Jy beam^{-1} , and Δv is the velocity channel width in km s^{-1} . Figure 1 shows an example μ_0 map for a rotational transition of Acetaldehyde in subplot (a). The μ_0 maps were compared with those created using `spectral-cube`⁷ as a sanity check. The average rms residuals between the two μ_0 maps across the entire set of observations for CH_3CHO , CH_3OH , and CH_3OCHO were $4.7 \times 10^{-5} \text{ Jy beam}^{-1} \text{ km s}^{-1}$, $9.6 \times 10^{-9} \text{ Jy beam}^{-1} \text{ km s}^{-1}$, and $4.0 \times 10^{-3} \text{ Jy beam}^{-1} \text{ km s}^{-1}$, respectively.

4.3.2. Moment 1 Maps

The first moment (μ_1) quantifies the velocity-weighted integrated line intensity, and is calculated by setting $n = 1$ in Equation 4 and normalizing it with the total integrated line intensity,

$$\mu_1 = \int_{-\infty}^{\infty} v I(v) dv / \int_{-\infty}^{\infty} I(v) dv. \quad (7)$$

Discretizing the equation once again, and substituting the known expression for μ_0 (see Equation 5), the average velocity of the emission line profile is

$$\langle v \rangle = \sum_{-\infty}^{\infty} v I(v) \Delta v / W. \quad (8)$$

Figure 1 shows an example μ_1 map for a rotational transition of Acetaldehyde in subplot (b).

4.3.3. Moment 2 Maps

The second moment (μ_2) quantifies the line width or the velocity dispersion of the emission profile, and it calculated by setting $n = 2$ in Equation 4, and once again, normalizing it with the total integrated line intensity,

$$\mu_2 = \sqrt{\frac{\int_{-\infty}^{\infty} I(v) (v - [\int_{-\infty}^{\infty} v I(v) dv / \int_{-\infty}^{\infty} I(v) dv])^2}{\int_{-\infty}^{\infty} I(v) dv}}. \quad (9)$$

Discretizing the equation once more, and substituting the known expressions for μ_0 (see Equation 5) and μ_1 (see Equation 7), the velocity dispersion is

$$\langle v \rangle^{1/2} = \sqrt{\frac{\sum_{-\infty}^{\infty} I(v) (v - \langle v \rangle)^2 \Delta v}{W}}. \quad (10)$$

Figure 1 shows an example μ_2 map for a rotational transition of Acetaldehyde in subplot (c).

4.4. Population Diagram

If the molecular emission is optically thin and in local thermodynamic equilibrium (LTE), the total column density of a molecular species can be expressed as

Table 3
Summary of Partition Functions

	CH_3CHO	CH_3OH	CH_3OCHO
Data			
T	$Q(T)$		
9.375	270.1167	19.5433	720.82
18.75	760.2458	68.7464	2030.84
37.50	2154.5221	230.2391	5772.42
75.0	6495.8039	731.0698	17548.82
150.0	22892.2045	2437.7654	59072.96
225.0	50049.7231	5267.8635	121102.02
300.0	86841.0823	9473.1198	199602.70
ref:	JPL	JPL	CDMS
$Q(T) = aT^b$ Fit Parameters			
a	1.6 ± 0.1	0.13 ± 0.03	9.3 ± 0.4
b	1.91 ± 0.02	1.96 ± 0.04	1.748 ± 0.007

$$N_{\text{tot}} = \frac{N_{ul}^{\text{thin}}}{Q(T)} g_{ul} e^{-E_{ul}/kT_{\text{rot}}}, \quad (11)$$

where all excitation temperatures are equal and are coupled with the gas kinetic temperature.

A popular technique for analyzing molecular cloud gas properties is the “population diagram”, also called the “rotational diagram” (e.g., Bisschop et al. 2008). With detections of multiple molecular transitions that span a range in excitation energies, this method consists of plotting the natural logarithm of the column density per statistical weight of each molecular energy level as a function of their upper-level energy. If the gas is optically thin and in local thermodynamic equilibrium (LTE), this will be a Boltzmann distribution. Thus, a plot of the natural logarithm of N_{ul}^{thin}/g as a function of E_{ul} will yield a straight line whose slope is related to the rotational (excitation) temperature (T_{rot}) and whose y-intercept is related to the total column density of the molecular species (N_{tot}). Fitting a line representing the function

$$\ln \left(\frac{N_{ul}^{\text{thin}}}{g} \right) = \ln \left(\frac{N_{\text{tot}}}{Z(T_{\text{rot}})} \right) - \left(\frac{E_{ul}}{k} \right) \frac{1}{T_{\text{rot}}} \quad (12)$$

allows for a direct measure of these quantities. The partition function, $Q(T)$, was determined by fitting the function $Q(T) = aT^b$ to publicly available partition function data from the JPL and CDMS catalogs using the Python Scipy `curve_fit` routine⁸ (used hereafter for all fitting procedures). With detections having temperatures of up to $\sim 2,500 \text{ K}$, this fit assumes that the partition function exhibits the same behaviour beyond 300 K . A more in-depth routine might include calculating the partition function rather than fitting it for $0 \text{ K} < T < 300 \text{ K}$ and extrapolating it to $2,500 \text{ K}$. Table 3 summarizes the partition function details, including the data used and the fitting results. Figure 2 shows the partition function fit obtained for acetaldehyde (red), methanol (blue), and methyl formate (purple), with the fit overlaid (black).

To use the population diagram technique for determining rotational temperatures and total molecular column

⁷ <http://spectral-cube.readthedocs.org/en/latest/moments.html>

⁸ <http://www.scipy.org/>

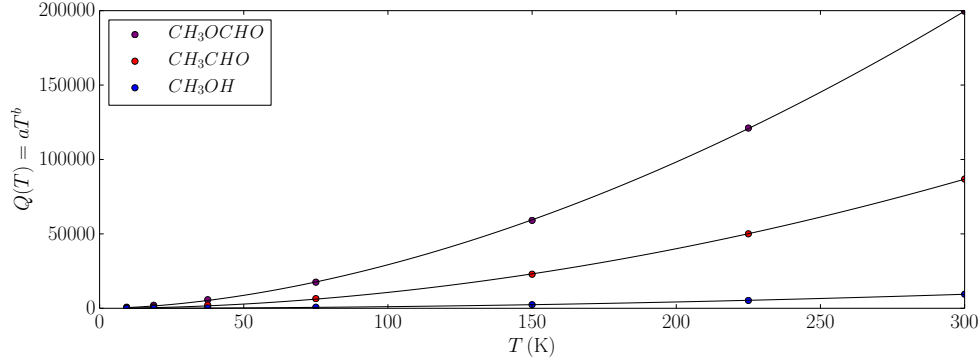


Figure 2. The partition function data shown with circles for acetaldehyde (red), methanol (blue), and methyl formate (purple) and the corresponding $Q(T) = aT^b$ fit overlaid in black.

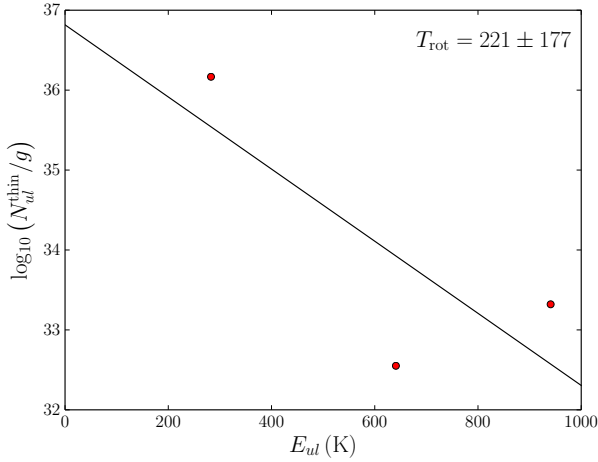


Figure 3. A representative population diagram for acetaldehyde with the fit overlaid that results in $T_{\text{rot}} = 221$ K and $N_{\text{tot}} = 4.75 \times 10^{20} \text{ cm}^{-2}$ located at the spatial pixel (132,133).

densities, the column densities of each upper-level energy transition were first calculated following

$$N_{ul}^{\text{thin}} = \frac{W 4\pi d^2}{10^{26} h c A_{ul} \Omega}. \quad (13)$$

Here, W is the integrated line intensity in $\text{Jy beam}^{-1} \text{ km s}^{-1}$ (see Equation 6), d is the distance to the source in parsecs, A_{ul} is the upper-level Einstein A coefficient, and Ω is the beam area in cm^2 which can be calculated using the major and minor axes of the beam size (θ_{maj} and θ_{min} , respectively) as

$$\Omega = \frac{\pi \theta_{\text{min}} \theta_{\text{maj}}}{4 \log 2}. \quad (14)$$

Figure 1 shows an example N_{ul}^{thin} map for a rotational transition of Acetaldehyde in subplot (d).

The total column density (N_{tot}) of the molecular species were then determined by applying a fit to Equation 12 and calculating the y-intercept. Figure 4 shows the resulting N_{tot} maps of (a) acetaldehyde, (b) methanol, and (c) methyl formate. The same fit was used to determine the rotational temperature (T_{rot}) of the molecular species by calculating the inverse of the

slope. Figure 5 shows the resulting T_{rot} maps of (a) acetaldehyde, (b) methanol, and (c) methyl formate. The regions where the population diagram technique was applied are those where there were at least two 5σ detections of rotational transitions in W with upper-level energies separated by at least 50 K to ensure that Equation 12 could be fit (i.e., you cannot fit a line to a single point). The T_{rot} and N_{tot} maps are restricted to regions satisfying $0.0 \text{ K} < T_{\text{rot}} < 2500 \text{ K}$ (this is discussed in more detail in Section 5.2).

5. DISCUSSION

Here we discuss the results of IRAS 1624 that were analyzed using the Python pipeline, starting with the moment maps, followed by the N_{tot} and T_{rot} maps, and finishing with future work.

5.1. Moment Maps

In this section, we will discuss the W , $\langle v \rangle$, and $\langle v \rangle^{1/2}$ maps which correspond to the μ_0 , μ_1 , and μ_2 moment maps, respectively. Results in this section are from all detections above the 5σ level in W at each spatial pixel for all rotational transitions of each molecule. For acetaldehyde, this corresponds to 6,619 detections, for methanol 2,301 detections, and for methyl formate 2,904 detections.

The distributions in W are very similar for all three molecules. The median values for emission are $0.67 \text{ Jy beam}^{-1} \text{ km s}^{-1}$, $0.47 \text{ Jy beam}^{-1} \text{ km s}^{-1}$, and $0.69 \text{ Jy beam}^{-1} \text{ km s}^{-1}$ for acetaldehyde, methanol, and methyl formate, respectively. The median values for absorption are $-0.76 \text{ Jy beam}^{-1} \text{ km s}^{-1}$, $-0.70 \text{ Jy beam}^{-1} \text{ km s}^{-1}$, and $-1.01 \text{ Jy beam}^{-1} \text{ km s}^{-1}$ for acetaldehyde, methanol, and methyl formate, respectively. Values in W are found to be as low as $-4.81 \text{ Jy beam}^{-1} \text{ km s}^{-1}$ and as high as $6.72 \text{ Jy beam}^{-1} \text{ km s}^{-1}$, which are likely being affected by blending with crowded emission lines. The distributions of W are shown at the top of Figure 6.

As discussed in Section 4.2, both acetaldehyde and methanol were found at a source velocity of $v_{\text{LSR}} = 2.7 \text{ km s}^{-1}$, while methyl formate was located at $v_{\text{LSR}} = 4.7 \text{ km s}^{-1}$. Acetaldehyde and methanol, therefore, have similar $\langle v \rangle$ distributions which themselves are different than that of methyl formate. Acetaldehyde is found to have a median source velocity of 2.5 km s^{-1} , while methanol has a median source velocity of 2.8

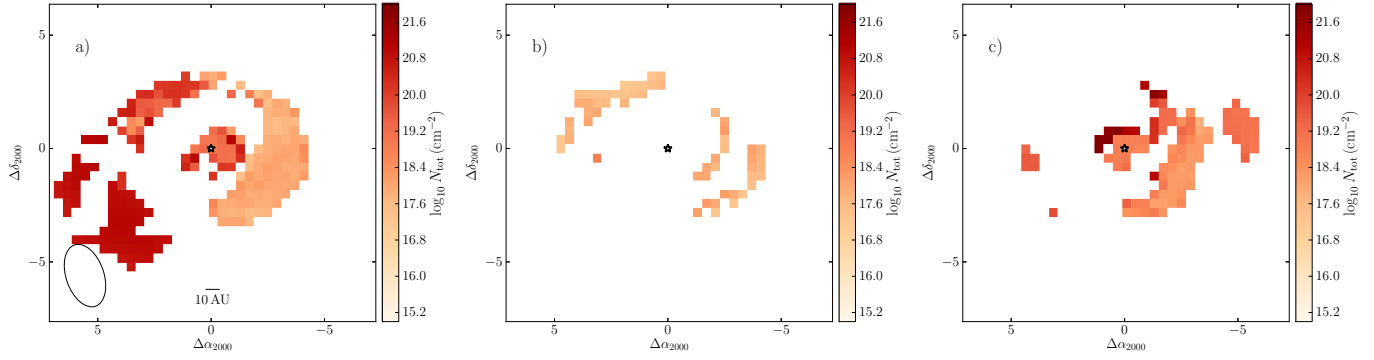


Figure 4. Total column density (N_{tot}) maps for (a) acetaldehyde, (b) methanol, and (c) methyl formate. The (black) star symbol indicates the pointing position of the IRAS B protostar and the approximate ALMA beam is shown in the bottom left corner. The spatial regions of the map are shown for those where $0.0 \text{ K} < T_{\text{rot}} < 2500 \text{ K}$ and correspond to the same regions shown in Figure 5 (above).

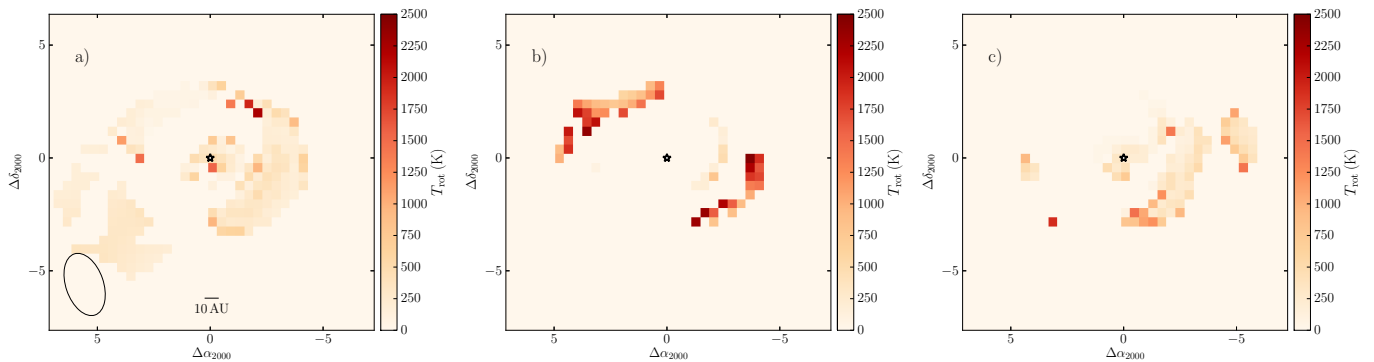


Figure 5. Rotational temperature (T_{rot}) maps for (a) acetaldehyde, (b) methanol, and (c) methyl formate. The (black) star symbol indicates the pointing position of the IRAS B protostar and the approximate ALMA beam is shown in the bottom left corner. The spatial regions of the map are shown for those where $0.0 \text{ K} < T_{\text{rot}} < 2500 \text{ K}$.

km s^{-1} . Methyl formate, on the other hand, has a medium source velocity located at 4.6 km s^{-1} . Acetaldehyde and methanol also exhibit similar standard deviations of these distributions, 0.45 km s^{-1} and 0.46 km s^{-1} , respectively, while methyl formate has a higher standard deviation of 0.60 km s^{-1} . It seems therefore that acetaldehyde and methanol have similar v_{LSR} distributions while methyl formate is comparatively quite different. The distributions of $\langle v \rangle$ are shown in the middle of Figure 6. It seems likely that these features are the result of line-blending. A closer look at these features is required.

Despite the differences in the distributions of $\langle v \rangle$, the distributions in $\langle v \rangle^{1/2}$ are quite similar across the three molecules. Acetaldehyde, methanol, and methyl formate have median $\langle v \rangle^{1/2}$ values of 0.69 km s^{-1} , 0.65 km s^{-1} , and 0.72 km s^{-1} , with standard deviations of 0.19 km s^{-1} , 0.21 km s^{-1} , 0.19 km s^{-1} , respectively. While methyl formate's difference in $\langle v \rangle$ seems significant (see above), the similarities in $\langle v \rangle^{1/2}$ raises the question of how different the kinematics really are. A more detailed analysis on the source velocities of the molecules are required (e.g., more rigorous LTE modeling) to strengthen these findings. The distributions in $\langle v \rangle^{1/2}$ are shown in the bottom of Figure 6.

We also investigate the relationship between v_{LSR} and σ_v (using their respective moment maps) and the upper-level energy of the transition, as well as the relationship

between themselves. Similar to the findings of Jørgensen et al. (2011), we find no trend of v_{LSR} nor σ_v with the E_{ul} , shown in the top and middle of Figure 7, respectively. A plot of σ_v versus v_{LSR} however, shown in the bottom of Figure 7, shows an interesting structure whereby a positive correlation is seen for $v > v_{\text{LSR}}$ and an anti-correlation is seen for $v < v_{\text{LSR}}$ for each of the three molecules. These features are likely the result of line blending. A possibility to test this may be to decrease/increase the frequency range that defines each emission line to see if these features weaken/strengthen.

5.2. Column Density Maps and Rotational Temperature Maps

The acetaldehyde, methanol, and methyl formate rotational transitions span a wide range of column densities (N_{ul}^{thin}). Column densities are found as low as $10^{12.3} \text{ cm}^{-2}$ and as high as $10^{19.0} \text{ cm}^{-2}$, which is almost seven orders of magnitude. Acetaldehyde and methanol alone are found to trace gas that spans 5.5 and 5.8 orders of magnitude in column density, while methyl formate spans 3.5 orders of magnitude. Acetaldehyde and methyl formate have median N_{ul}^{thin} values of $10^{14.4} \text{ cm}^{-2}$ and $10^{15.3} \text{ cm}^{-2}$, respectively, while methanol has a lower median N_{ul}^{thin} value of $10^{13.5} \text{ cm}^{-2}$.

Figure 4 shows the N_{tot} maps for (a) acetaldehyde, (b) methanol, and (c) methyl formate. Section 4.4 discusses how the regions with detections were determined.

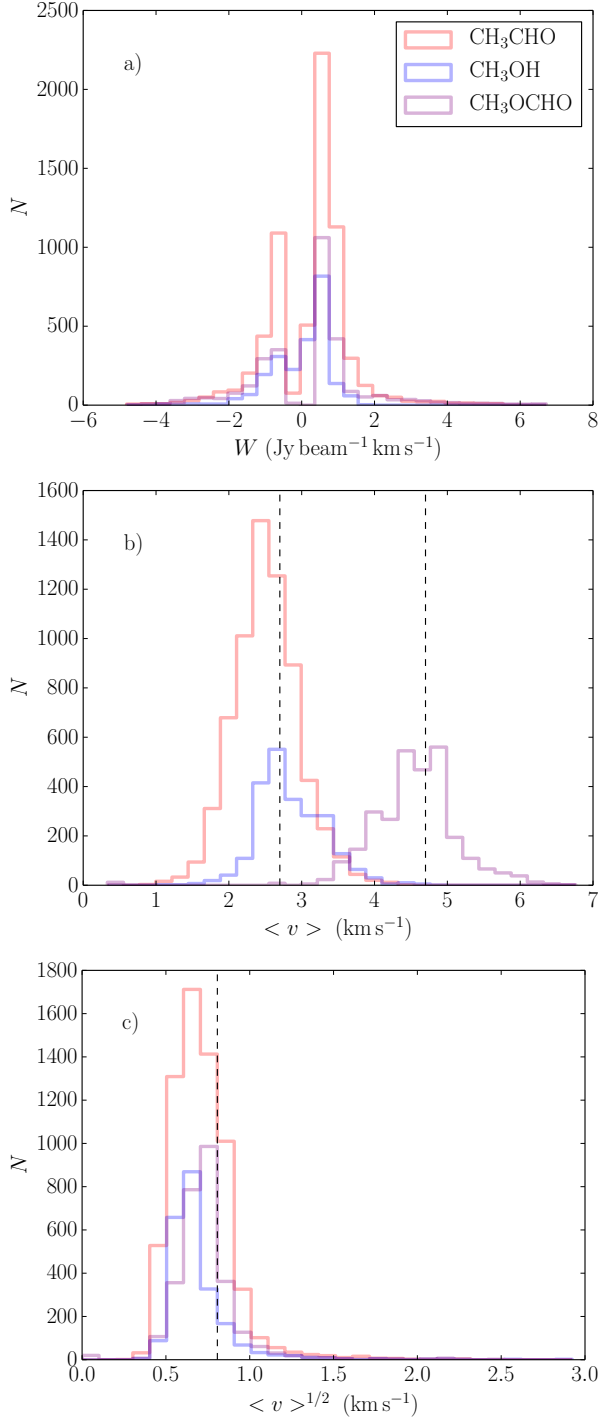


Figure 6. Distributions of (a) W , (b) $\langle v \rangle$, and (c) $\langle v \rangle^{1/2}$, corresponding to μ_0 , μ_1 , and μ_2 moment maps, respectively. Acetaldehyde is shown in red, methanol is shown in blue, and methyl formate is shown in purple.

It is clear that the three molecules are tracing gas in different spatial regions of IRAS B. While acetaldehyde and methyl formate have somewhat extended emission, methanol seems to trace more compact emission. This could, however, be due to the comparatively lower number of detections in methanol (18) than acetaldehyde (97) and methyl formate (50). The total column den-

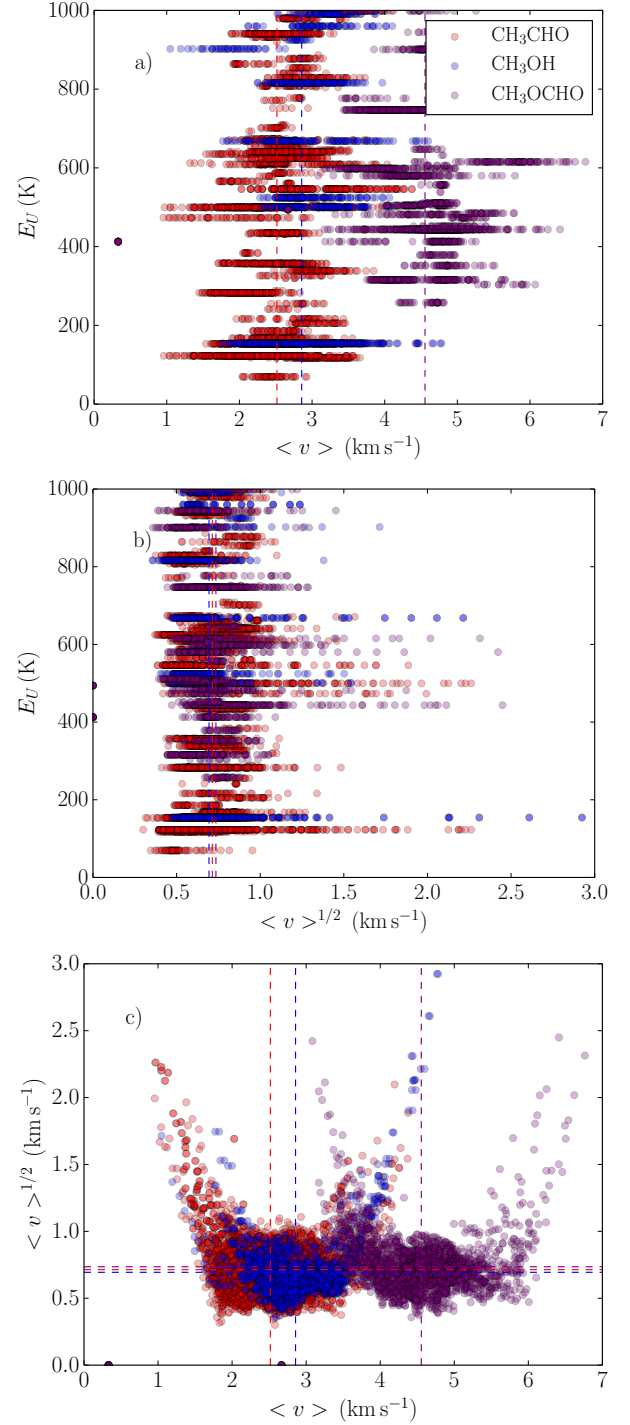


Figure 7. Correlation plots of (a) upper-level energy versus velocity, (b) upper-level energy versus velocity dispersion, and (c) velocity dispersion versus velocity for all 5 σ detections. Acetaldehyde is shown in red, methanol in blue, and methyl formate in purple.

sity of the molecules (N_{tot}) ranges from $10^{17.1} \text{ cm}^{-2}$ to $10^{22.3} \text{ cm}^{-2}$, which is approximately 5 orders of magnitude. Acetaldehyde and methyl formate spans 3.6 and 4.5 orders of magnitude, respectively, while methanol spans 1.7 orders of magnitude in N_{tot} . Acetaldehyde is found to have a median N_{tot} value of $10^{19.3} \text{ cm}^{-2}$, with $10^{17.7} \text{ cm}^{-2}$ and $10^{18.9} \text{ cm}^{-2}$ for methanol and methyl

formate, respectively. The observed column densities are quite high, and further investigation is required to better understand what may be causing these values to be so unusually high. While they are likely being affected by line blending, which is a significant obstacle with the extent of line crowding present in the data and requires more careful investigation and correction, this effect is unlikely to cause column densities several orders of magnitude higher than expected.

Figure 5 shows the T_{rot} maps for (a) acetaldehyde, (b) methanol, and (c) methyl formate. Rotational temperatures (T_{rot}) are found between 23 K and 2,451 K. In addition to each of the three molecules tracing gas with a range of column densities, there also is a wide range of rotational temperatures present. Acetaldehyde traces gas from 23 K to 2,228 K, while methanol traces gas from 94 K to 2,451 K and methyl formate from 49 K to 1,898 K. Acetaldehyde is found to trace a median T_{rot} of 254 K, with a median value of 1,189 K for methanol and 307 K for methyl formate. While the T_{rot} found for acetaldehyde is consistent with a previous combined JCMT and IRAM survey (Caux et al. 2011), further investigation on the large uncertainties in T_{rot} are required. While many spatial pixels result in “reasonable” T_{rot} values (see Figure 5), there still remain many regions with unphysical (i.e., negative) temperatures or large uncertainties. Using the quantum numbers to focus on specific K-ladders may help to elucidate this.

5.3. Future Work

The following are aspects of the pipeline that serve to be improvements in the future:

- Scanning all spectral baselines to measure the median sensitivity of each spatial pixel for more accurate noise maps.
- Calculating the partition function directly instead of fitting and interpolating to high temperature values.
- Implementing an automated way to correct for line blending.
- Creating population diagrams for specific K quantum numbers which may help to shed light on the non-physical temperatures and high uncertainties in the current pipeline. Understanding the format of the quantum numbers provided by the JPL and CDMS databases will be required (some have 2 or 3 quantum numbers instead of 4 and need to be separated properly).
- Investigate the (anti-) correlation seen in the σ_v versus v_{LSR} plot by increasing the frequency/velocity range of the spectral window used for the measurements of each emission line. If these (anti-) correlations strengthen (or weaken if the frequency range is decreased), these features are then likely the result of line blending.

6. SUMMARY

We construct a Python pipeline to analyse the high quality, spatially resolved ALMA data of the deeply-embedded low-mass protostar IRAS 16293-2422. In sum-

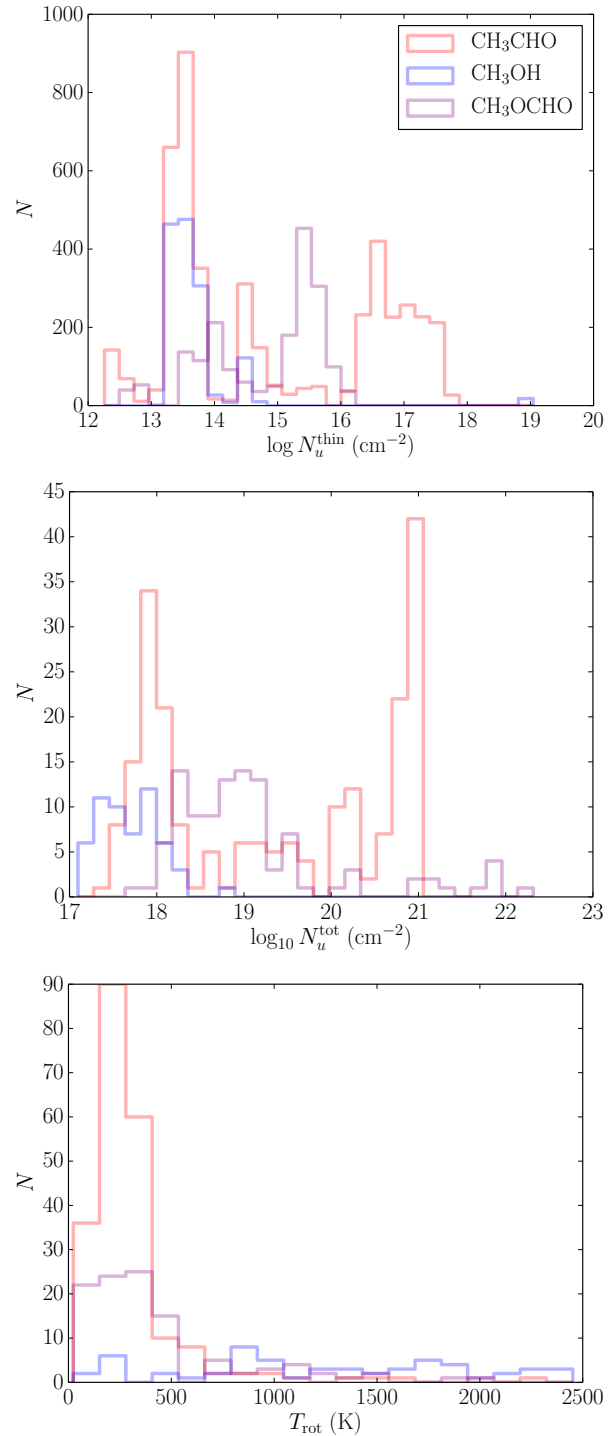


Figure 8. Distributions of (a) W , (b) $\langle v \rangle$, and (c) $\langle v \rangle^{1/2}$, corresponding to μ_0 , μ_1 , and μ_2 moment maps, respectively. Acetaldehyde is shown in red, methanol is shown in blue, and methyl formate is shown in purple.

mary, the steps that the Python pipeline performs are the following:

- Molecular lines were identified for pure rotational transitions present in the frequency ranges of each spw using the JPL and CDMS catalogs. Splatalogue was not used to query these database since

several emission lines were missing.

- Descriptors of the transition were obtained including the rest frequency (ν_0) of the transition, resolved quantum numbers of the transition, Einstein A coefficient of the upper-level (A_{ul}), the upper-level energy (E_{ul}), and the statistical weight of the upper level (g_{ul}).
- Noise maps were made using pre-defined frequency ranges specific for each spw.
- Using a source velocity (v_{LSR}) and velocity dispersion (σ) of the source, a spectral slab that is 1.5σ about the source v_{LSR} was obtained. We determine a source local standard-of-rest velocity of $v_{\text{LSR}} = 2.7 \text{ km s}^{-1}$ for acetaldehyde and methanol, and $v_{\text{LSR}} = 4.7 \text{ km s}^{-1}$ for methyl formate, using LTE modeling.
- The μ_0 , μ_1 , and μ_2 moment maps were calculated, corresponding to W , $\langle v \rangle$, and $\langle v \rangle^{1/2}$ maps, respectively. These maps were calculated by “brute force”, but the W map was also calculated using `spectral-cube` to investigate the residual variance between the two as a sanity check.
- Line blending was identified by eye and corrected using the A_{ul} and g_{ul} of each transition.
- The spatial pixel with the strongest W detection was used to visualize a spectrum representative for each detected transition.
- The column densities of each transition (N_{ul}^{thin}) were calculated using the W maps.
- The three moment maps (μ_0 , μ_1 , μ_2), the column density maps (N_{ul}^{thin}), and noise maps were saved to a FITS file for each transition. The spectrum corresponding to the strongest W detection was also saved to a FITS file for each transition (if applicable). Any useful information related to the transition and the source were added to the FITS header.
- Histograms of the three moment maps as well as column densities for all detections of rotational transitions above a 5σ level were made.
- Correlation plots of v_{LSR} and σ_v versus E_{ul} as v_{LSR} versus σ_v were made.
- Histograms of total column densities and rotational temperatures of the three molecules were made for spatial regions satisfying $0 \text{ K} < T_{\text{rot}} < 2,500 \text{ K}$ were made.

The following summarizes the results:

1. Using an LTE model, acetaldehyde and methanol were found to be located at a local standard-of-rest velocity of $v_{\text{LSR}} = 2.7 \text{ km s}^{-1}$, while methyl formate is located at $v_{\text{LSR}} = 4.7 \text{ km s}^{-1}$.
2. We detect 97/220 (44%) acetaldehyde, 18/32 (56%) methanol, and 50/116 (43%) methyl formate pure rotational transitions in IRAS B above the 5σ level.

3. The excitation energies detected with acetaldehyde range from 69.48 K to 998.81 K, methanol from 154.25 K to 990.87 K, and methyl formate from 257.75 K to 998.82 K.
4. Assuming a model for the partition function of $Q(T) = aT^b$, we determine $(1.6 \pm 0.1)T^{1.91 \pm 0.02}$ for acetaldehyde, $(0.13 \pm 0.03)T^{1.96 \pm 0.04}$ for methanol, and $(9.3 \pm 0.4)T^{1.748 \pm 0.007}$ for methyl formate.
5. While acetaldehyde and methyl formate have somewhat extended emission, methanol is found to be more compact. This may however be due to the lower number of detections in methanol.
6. Despite the differences in the distributions of v_{LSR} , all three molecules have very similar distributions in σ_v . Acetaldehyde, methanol, and methyl formate have median v_{LSR} values of 2.5 km s^{-1} , 2.8 km s^{-1} , 4.6 km s^{-1} , respectively. Acetaldehyde, methanol, and methyl formate have median $\langle v \rangle^{1/2}$ values of 0.69 km s^{-1} , 0.65 km s^{-1} , and 0.72 km s^{-1} , with standard deviations of 0.19 km s^{-1} , 0.21 km s^{-1} , 0.19 km s^{-1} , respectively.
7. We find no correlation between E_{ul} and v_{LSR} nor E_{ul} and σ_v .
8. We find a correlation between σ_v and v_{LSR} for $v > v_{\text{LSR}}$ and an anti-correlation for $v < v_{\text{LSR}}$ that is likely the result of line blending.
9. The total column densities N_{tot} found were higher than those in previous studies. Line blending and ALMA’s comparatively small beam size do not alone explain the high N_{tot} found in this analysis, and requires further investigation.
10. Acetaldehyde was found to have a median T_{rot} of 254 K, which is consistent is previous studies. Methanol and methyl formate were found to have median T_{rot} values of 1,189 K and 307 K, respectively.

REFERENCES

- Andre, P., Ward-Thompson, D., & Barsony, M. 1993, *ApJ*, 406, 122 [2](#)
- Bisschop, S. E., Jørgensen, J. K., Bourke, T. L., Bottinelli, S., & van Dishoeck, E. F. 2008, *A&A*, 488, 959 [1](#), [1](#), [2](#), [4.4](#)
- Bisschop, S. E., Jørgensen, J. K., van Dishoeck, E. F., & de Wachter, E. B. M. 2007, *A&A*, 465, 913
- Blake, G. A., van Dishoeck, E. F., Jansen, D. J., Groesbeck, T. D., & Mundy, L. G. 1994, *ApJ*, 428, 680
- Bottinelli, S., Ceccarelli, C., Neri, R., et al. 2004, *ApJ*, 617, L69
- Caux, E., Kahane, C., Castets, A., et al. 2011, *A&A*, 532, A23 [5.2](#)
- Cazaux, S., Tielens, A. G. G. M., Ceccarelli, C., et al. 2003, *ApJ*, 593, L51 [1](#)
- Chandler, C. J., Brogan, C. L., Shirley, Y. L., & Loinard, L. 2005, *ApJ*, 632, 371 [1](#), [2](#)
- Favre, C., Jørgensen, J. K., Field, D., et al. 2014, *ApJ*, 790, 55
- Goldsmith, P. F., & Langer, W. D. 1999, *ApJ*, 517, 209
- Herbst, E., & van Dishoeck, E. F. 2009, *Annual Review of Astronomy and Astrophysics*, 47, 427 [1](#)
- Jørgensen, J. K., Bourke, T. L., Nguyen Luong, Q., & Takakuwa, S. 2011, *A&A*, 534, A100 [2](#), [4.2](#), [4.2](#), [4.2](#), [5.1](#)
- Jørgensen, J. K., Favre, C., Bisschop, S. E., et al. 2012, *ApJ*, 757, L4

- Kristensen, L. E., Klaassen, P. D., Mottram, J. C., Schmalzl, M., & Hogerheijde, M. R. 2013, *A&A*, 549, L6
- Mundy, L. G., Myers, S. T., & Wilking, B. A. 1986, *ApJ*, 311, L75 [2](#)
- Mundy, L. G., Wootten, A., Wilking, B. A., Blake, G. A., & Sargent, A. I. 1992, *ApJ*, 385, 306 [2](#)
- Myers, P. C. 1985, in *Protostars and Planets II*, ed. D. C. Black & M. S. Matthews, 81–103 [1](#)
- Padgett, D. L., Rebull, L. M., Stapelfeldt, K. R., et al. 2008, *ApJ*, 672, 1013
- Pech, G., Loinard, L., Chandler, C. J., et al. 2010, *ApJ*, 712, 1403
- Persson, M. V., Jørgensen, J. K., & van Dishoeck, E. F. 2013, *A&A*, 549, L3
- Pineda, J. E., Maury, A. J., Fuller, G. A., et al. 2012, *A&A*, 544, L7 [2](#)
- Stark, R., Sandell, G., Beck, S. C., et al. 2004, *ApJ*, 608, 341 [2](#)
- van der Tak, F. F. S., van Dishoeck, E. F., & Caselli, P. 2000, *A&A*, 361, 327 [1](#)
- Walker, C. K., Lada, C. J., Young, E. T., Maloney, P. R., & Wilking, B. A. 1986, *ApJ*, 309, L47 [2](#)
- Walker, C. K., Lada, C. J., Young, E. T., & Margulis, M. 1988, *ApJ*, 332, 335 [2](#)
- Walmsley, C. M., Cesaroni, R., Churchwell, E., & Hofner, P. 1992, in *Astronomische Gesellschaft Abstract Series*, Vol. 7, *Astronomische Gesellschaft Abstract Series*, ed. G. Klare, 93 [1](#)
- Wootten, A. 1989, *ApJ*, 337, 858 [2](#)

APPENDIX

Tables [A.1](#), [A.2](#), and [A.3](#) lists all of the detections in IRAS B for acetaldehyde, methanol, and methyl formate, respectively.

Table A.1
Detected Acetaldehyde Transitions

ν_0 (GHz) (1)	QN (2)	A_{ul} (s^{-1}) (3)	E_{ul} (K) (4)	g (5)	SNR _{max} (6)	linelist (7)
spw 0a						
703.2674413	(21-814-1)	1.01×10^{-03}	357.84	86.0	7.9	JPL
703.358083	(15-8-7-2)	8.70×10^{-04}	255.24	62.0	6.6	JPL
703.3604509	(7-3-5-6)	1.64×10^{-07}	432.65	30.0	6.4	JPL
703.4146951	(14-8-6-2)	8.31×10^{-04}	241.37	58.0	5.4	JPL
703.4234917	(20-813-1)	9.93×10^{-04}	338.41	82.0	15.3	JPL
703.4763984	(1312-2-7)	1.67×10^{-05}	771.38	54.0	5.3	JPL
703.4972505	(36-729-5)	1.42×10^{-06}	931.67	146.0	12.6	JPL
703.4992213	(12-8-4-2)	7.25×10^{-04}	216.41	50.0	12.7	JPL
703.5296091	(11-8-3-2)	6.50×10^{-04}	205.31	46.0	9.2	JPL
703.5577029	(271216-3)	1.43×10^{-07}	875.79	110.0	5.7	JPL
703.5602546	(19-812-1)	9.75×10^{-04}	319.92	78.0	5.4	JPL
703.5679305	(29-624-6)	3.85×10^{-05}	863.95	118.0	6.6	JPL
703.5721401	(9-8-1-2)	4.26×10^{-04}	185.89	38.0	6.6	JPL
703.6854865	(24-420-8)	4.09×10^{-04}	693.01	98.0	5.2	JPL
703.712346	(12-8-4-8)	6.97×10^{-04}	608.77	50.0	19.0	JPL
703.7154183	(14-6-9-7)	7.71×10^{-04}	546.14	58.0	6.6	JPL
703.8534774	(29-821-3)	1.11×10^{-03}	751.64	118.0	5.8	JPL
703.929342	(37-533-1)	4.94×10^{-07}	708.33	150.0	5.9	JPL
703.9480303	(15-8-8-1)	8.72×10^{-04}	255.17	62.0	5.6	JPL
704.0127544	(14-8-7-1)	8.33×10^{-04}	241.3	58.0	6.3	JPL
704.0475697	(14-311-2)	2.90×10^{-07}	117.68	58.0	9.8	JPL
704.1129288	(12-8-5-1)	7.27×10^{-04}	216.33	50.0	7.6	JPL
704.1467188	(15-313-6)	7.93×10^{-04}	518.14	62.0	5.2	JPL
spw 0b						
704.2068482	(9-8-2-1)	4.27×10^{-04}	185.81	38.0	8.1	JPL
704.4741384	(221310-3)	1.16×10^{-04}	815.26	90.0	3.1	JPL
704.4741837	(2213-9-3)	1.16×10^{-04}	815.26	90.0	3.1	JPL
704.5071697	(27-622-7)	7.30×10^{-07}	804.54	110.0	5.4	JPL
704.6226564	(14-510-1)	9.15×10^{-08}	153.5	58.0	5.4	JPL
spw 1a						
691.4620264	(40-931-0)	1.36×10^{-06}	940.77	162.0	59.2	JPL
691.6475366	(1912-7-0)	9.96×10^{-05}	499.72	78.0	5.7	JPL
691.6475366	(1912-8-0)	9.96×10^{-05}	499.72	78.0	5.7	JPL
691.8446593	(29-425-3)	3.77×10^{-05}	644.92	118.0	11.2	JPL
691.887779	(14-510-0)	8.59×10^{-04}	153.6	58.0	12.6	JPL
691.9296543	(14-5-9-0)	8.59×10^{-04}	153.6	58.0	11.4	JPL
spw 1b						
690.388632	(26-323-2)	4.25×10^{-08}	348.37	106.0	5.9	JPL
690.3989118	(11-3-8-5)	2.17×10^{-06}	287.95	46.0	5.7	JPL
690.4831507	(1010-0-6)	8.86×10^{-06}	641.82	42.0	4.4	JPL
690.4831548	(1010-1-6)	8.86×10^{-06}	641.82	42.0	4.4	JPL
690.5002063	(31-823-3)	1.57×10^{-06}	808.09	126.0	6.6	JPL
690.5155439	(291118-3)	2.73×10^{-07}	877.81	118.0	6.8	JPL
690.561295	(9-6-3-2)	1.28×10^{-03}	122.83	38.0	0.5	JPL
690.5613178	(1912-7-2)	9.92×10^{-05}	499.73	78.0	12.1	JPL
690.5622734	(1912-8-1)	9.91×10^{-05}	499.65	78.0	13.5	JPL
690.6127641	(40-932-1)	8.63×10^{-07}	940.77	162.0	7.8	JPL
690.6328608	(36-235-7)	1.81×10^{-03}	998.81	146.0	9.4	JPL
690.7501916	(31-824-3)	1.57×10^{-06}	808.09	126.0	7.2	JPL
690.7968112	(25-620-3)	9.24×10^{-07}	586.28	102.0	8.4	JPL
690.8370144	(37-136-3)	1.42×10^{-03}	854.02	150.0	9.2	JPL
690.8847803	(13-4-9-5)	1.16×10^{-06}	326.36	54.0	6.7	JPL
690.8869475	(42-835-1)	5.43×10^{-04}	979.7	170.0	6.8	JPL
690.907316	(42-834-0)	1.12×10^{-03}	979.68	170.0	8.3	JPL
690.9331842	(1912-8-4)	9.58×10^{-05}	701.6	78.0	10.1	JPL
690.9628201	(30-327-5)	1.35×10^{-05}	661.61	122.0	7.4	JPL
690.9888607	(42-834-2)	5.43×10^{-04}	979.73	170.0	9.5	JPL
691.0031648	(37-136-0)	1.50×10^{-03}	648.54	150.0	5.3	JPL
691.1268018	(291119-3)	2.74×10^{-07}	877.81	118.0	7.4	JPL
691.1855252	(14-510-1)	8.55×10^{-04}	153.5	58.0	13.1	JPL
spw 2a						
689.5659133	(27-424-6)	4.70×10^{-06}	777.48	110.0	6.5	JPL
689.7399502	(12-6-7-3)	4.76×10^{-07}	356.99	50.0	5.6	JPL
689.8727243	(23-419-8)	4.91×10^{-04}	670.87	94.0	11.9	JPL
690.0854133	(31-626-6)	3.33×10^{-05}	919.61	126.0	5.5	JPL
690.1384977	(7-6-2-7)	7.34×10^{-06}	473.32	30.0	14.3	JPL

Table A.1 — *Continued*

ν_0 (GHz) (1)	QN (2)	A_{ul} (s^{-1}) (3)	E_{ul} (K) (4)	g (5)	SNR _{max} (6)	linelist (7)
spw 2b						
688.7285086	(20-417-3)	5.81×10^{-04}	434.55	82.0	7.2	JPL
688.8136594	(12-6-6-2)	1.98×10^{-07}	153.35	50.0	13.5	JPL
688.8157492	(8-4-4-0)	2.69×10^{-07}	69.48	34.0	19.9	JPL
688.8243725	(35-332-3)	1.13×10^{-02}	816.95	142.0	17.1	JPL
688.9303113	(35-332-2)	1.13×10^{-02}	612.21	142.0	6.3	JPL
688.9584768	(35-332-0)	1.13×10^{-02}	612.24	142.0	14.9	JPL
688.9632471	(18-612-8)	1.05×10^{-03}	624.63	74.0	11.4	JPL
688.9854284	(27-324-3)	7.03×10^{-06}	578.64	110.0	6.9	JPL
689.1341535	(9-6-4-0)	1.27×10^{-03}	122.83	38.0	7.1	JPL
689.1341575	(9-6-3-0)	1.27×10^{-03}	122.83	38.0	7.1	JPL
689.1573844	(36-135-6)	1.09×10^{-02}	998.01	146.0	6.7	JPL
689.1579412	(14-312-6)	7.59×10^{-04}	504.2	58.0	7.0	JPL
689.2391387	(1311-2-3)	3.29×10^{-05}	560.05	54.0	3.1	JPL
689.2391387	(1311-3-3)	3.29×10^{-05}	560.05	54.0	3.1	JPL
689.3221372	(9-6-4-1)	1.27×10^{-03}	122.74	38.0	22.7	JPL
spw 3a						
687.4500303	(241312-1)	1.35×10^{-04}	657.43	98.0	8.2	JPL
687.5427143	(36-334-1)	1.12×10^{-02}	635.11	146.0	8.7	JPL
687.5529116	(36-334-0)	1.12×10^{-02}	635.14	146.0	8.0	JPL
687.7673755	(18-415-7)	6.96×10^{-07}	565.88	74.0	12.8	JPL
687.8159585	(15-511-1)	1.15×10^{-07}	167.39	62.0	27.1	JPL
688.0564493	(35-233-8)	1.22×10^{-04}	977.15	142.0	6.5	JPL
688.1534792	(14-510-3)	8.22×10^{-04}	356.91	58.0	5.9	JPL
688.2013956	(14-5-9-3)	8.22×10^{-04}	356.91	58.0	10.2	JPL
688.2256957	(36-334-3)	1.13×10^{-02}	840.15	146.0	7.1	JPL
spw 3b						
686.5428225	(17-413-5)	2.43×10^{-06}	383.71	70.0	7.3	JPL
686.5805758	(1511-4-5)	6.22×10^{-05}	587.42	62.0	8.5	JPL
687.0340342	(9-4-6-4)	1.20×10^{-07}	282.78	38.0	43.1	JPL
687.0378884	(35-530-2)	1.33×10^{-06}	640.96	142.0	55.8	JPL
687.1006031	(8-8-0-6)	1.56×10^{-03}	546.25	34.0	18.9	JPL
687.1006031	(8-8-1-6)	1.56×10^{-03}	546.25	34.0	18.9	JPL
687.119142	(35-431-0)	1.12×10^{-02}	623.62	142.0	6.2	JPL
687.1255008	(35-431-5)	1.12×10^{-02}	829.02	142.0	9.8	JPL
687.1533879	(35-431-2)	1.12×10^{-02}	623.6	142.0	13.9	JPL
687.1831706	(30-625-7)	6.30×10^{-07}	886.54	122.0	5.3	JPL
687.3157423	(36-532-1)	7.73×10^{-07}	673.95	146.0	9.9	JPL

Table A.2
Detected Methanol Transitions

ν_0 (GHz) (1)	QN (2)	A_{ul} (s^{-1}) (3)	E_{ul} (K) (4)	g (5)	SNR _{max} (6)	linelist (7)
spw 0b						
704.288957	(20-2-0)	7.40×10^{-04}	524.45	41.0	9.1	JPL
704.580556	(28-3-0)	6.53×10^{-04}	990.87	57.0	13.4	JPL
704.998817	(26-1-0)	1.34×10^{-04}	816.22	53.0	9.1	JPL
704.288757	(20-2-19-0)	7.13×10^{-04}	816.22	41.0	9.2	CDMS
704.999279	(26-1-26-0)	1.34×10^{-04}	816.22	53.0	9.1	CDMS
spw 1a						
691.645051	(8-3-1)	1.87×10^{-03}	500.74	17.0	11.8	JPL
691.645159	(8-3-6-1)	1.88×10^{-03}	500.74	17.0	11.8	CDMS
spw 1b						
690.596799	(14-1-2)	2.71×10^{-09}	925.05	29.0	7.1	JPL
spw 2a						
689.874613	(15-8-1)	3.27×10^{-04}	959.87	62.0	6.0	JPL
689.874411	(15-8-7-1)	3.30×10^{-04}	959.87	31.0	3.0	CDMS
689.874411	(15-8-8-1)	3.30×10^{-04}	959.87	31.0	3.0	CDMS
spw 2b						
689.205784	(23-2-0)	9.87×10^{-05}	668.11	47.0	7.0	JPL
689.205906	(23-2-22-0)	9.88×10^{-05}	668.11	47.0	7.0	CDMS
spw 3a						
687.751712	(20-3-1)	8.01×10^{-07}	902.33	41.0	13.8	JPL
spw 3b						
686.731501	(9-3-0)	1.34×10^{-03}	154.25	19.0	23.3	JPL
687.224595	(9-3-0)	1.34×10^{-03}	154.25	19.0	21.1	JPL
686.731459	(9-3-7-0)	1.34×10^{-03}	154.25	19.0	46.6	CDMS
687.224558	(9-3-6-0)	1.34×10^{-03}	154.25	19.0	21.1	CDMS

Table A.3
Detected Methyl Formate Transitions

ν_0 (GHz) (1)	QN (2)	A_{ul} (s^{-1}) (3)	E_{ul} (K) (4)	g (5)	SNR _{max} (6)	linelist (7)
spw 0a						
703.883369	(2017-3-5)	7.42×10^{-04}	504.5	82.0	8.9	JPL
704.1472212	(1818-0-2)	8.74×10^{-04}	315.71	74.0	6.2	JPL
spw 0b						
704.1938838	(1818-0-0)	8.74×10^{-04}	315.73	74.0	14.3	JPL
704.1938838	(1818-1-0)	8.74×10^{-04}	315.73	74.0	14.3	JPL
704.2105977	(1818-1-1)	8.74×10^{-04}	315.71	74.0	6.5	JPL
704.215394	(31-625-5)	2.71×10^{-05}	510.84	126.0	7.4	JPL
704.6159634	(341421-0)	1.18×10^{-05}	481.62	138.0	6.5	JPL
704.6214434	(341420-0)	1.18×10^{-05}	481.62	138.0	6.0	JPL
704.6376611	(341420-2)	1.18×10^{-05}	481.62	138.0	10.6	JPL
704.6575988	(341421-1)	1.18×10^{-05}	481.61	138.0	6.2	JPL
704.8536775	(391426-3)	1.51×10^{-05}	776.61	158.0	6.0	JPL
spw 1a						
691.4684977	(27-721-4)	2.37×10^{-05}	443.61	110.0	71.9	JPL
spw 1b						
690.3326038	(381029-1)	2.07×10^{-04}	507.68	154.0	7.3	JPL
690.794583	(361027-4)	1.34×10^{-04}	647.23	146.0	7.1	JPL
690.891259	(27-721-1)	2.54×10^{-05}	257.75	110.0	7.5	JPL
690.9317949	(27-721-0)	2.54×10^{-05}	257.75	110.0	6.9	JPL
691.1293545	(33-726-5)	6.14×10^{-05}	556.75	134.0	7.9	JPL
691.183207	(421230-0)	9.20×10^{-06}	632.06	170.0	5.8	JPL
spw 2a						
689.429813	(331122-2)	1.89×10^{-04}	412.75	134.0	2.1	JPL
689.8190169	(401426-2)	1.45×10^{-05}	615.36	162.0	10.7	JPL
689.9169232	(401426-0)	1.69×10^{-05}	615.35	162.0	5.7	JPL
690.060891	(27-721-3)	2.36×10^{-05}	443.53	110.0	5.6	JPL
690.1071502	(331122-5)	2.91×10^{-04}	598.4	134.0	8.9	JPL
690.3326038	(381029-1)	2.07×10^{-04}	507.68	154.0	5.6	JPL
spw 2b						
688.5085152	(2116-5-3)	6.25×10^{-04}	494.01	86.0	13.7	JPL
688.5085152	(2116-6-3)	6.25×10^{-04}	494.01	86.0	13.7	JPL
688.7229288	(33-825-0)	5.50×10^{-05}	378.68	134.0	6.0	JPL
688.7314843	(33-825-2)	5.50×10^{-05}	378.67	134.0	6.8	JPL
689.007361	(531142-0)	4.86×10^{-03}	944.47	214.0	6.6	JPL
689.0075167	(1917-3-1)	7.30×10^{-04}	303.7	78.0	6.6	JPL
689.016652	(441430-3)	1.92×10^{-05}	900.69	178.0	13.5	JPL
689.0172979	(531142-2)	4.86×10^{-03}	944.46	214.0	14.0	JPL
689.0373196	(331123-1)	1.89×10^{-04}	412.74	134.0	9.0	JPL
689.0413446	(411032-1)	1.83×10^{-04}	580.13	166.0	15.4	JPL
689.1271072	(331122-2)	1.01×10^{-04}	412.75	134.0	6.0	JPL
689.1373441	(331123-4)	2.89×10^{-04}	598.25	134.0	11.5	JPL
689.3400254	(331123-1)	1.01×10^{-04}	412.74	134.0	7.2	JPL
689.3614293	(281316-3)	4.01×10^{-04}	538.51	114.0	5.6	JPL
689.3614434	(281315-3)	4.01×10^{-04}	538.51	114.0	5.6	JPL
689.3914693	(331122-0)	2.90×10^{-04}	412.75	134.0	14.1	JPL
spw 3a						
687.45209	(37-929-0)	5.50×10^{-06}	473.31	150.0	7.2	JPL
687.7550027	(441431-3)	1.91×10^{-05}	900.69	178.0	6.1	JPL
687.7756557	(36-927-2)	1.58×10^{-04}	451.83	146.0	15.2	JPL
688.1598376	(281316-0)	3.97×10^{-04}	351.86	114.0	6.4	JPL
688.1598597	(281315-0)	3.97×10^{-04}	351.86	114.0	6.4	JPL
688.1653989	(281316-1)	3.97×10^{-04}	351.85	114.0	8.0	JPL
688.2255156	(35-827-5)	1.00×10^{-04}	605.87	142.0	5.7	JPL
spw 3b						
686.538586	(541341-0)	4.72×10^{-03}	998.82	218.0	9.9	JPL
686.5431895	(371028-0)	2.13×10^{-04}	484.79	150.0	7.2	JPL
687.0396517	(471037-0)	1.13×10^{-05}	747.03	190.0	53.3	JPL